International Journal of Pharmaceutics 593 (2021) 120097

Contents lists available at ScienceDirect

International Journal of Pharmaceutics

journal homepage: www.elsevier.com/locate/ijpharm

3D-printed platform multi-loaded with bioactive, magnetic nanoparticles and an antibiotic for re-growing bone tissue

Ana S. Saraiva [a], Isabel A.C. Ribeiro [a], Maria H. Fernandes [b,c], Ana Cláudia Cerdeira [d], Bruno J. C. Vieira [d], João Carlos Waerenborgh [d], Laura C.J. Pereira [d], Ricardo Cláudio [e,f], Maria João Carmezim [e,g], Pedro Gomes [b,c], Lídia M. Gonçalves [a], Catarina F. Santos [e,g,1,*], Ana F. Bettencourt [a,1,*]

[a] Research Institute for Medicines (iMed.ULisboa), Faculty of Pharmacy, Universidade de Lisboa, Avenida Prof. Gama Pinto, 1649-003 Lisboa, Portugal
[b] Laboratory for Bone Metabolism and Regeneration – Faculty of Dental Medicine, U. Porto, Portugal
[c] REQUIMTE/LAQV – Universidade do Porto, Porto, Portugal
[d] C2TN, DECN, Instituto Superior Técnico, Universidade de Lisboa, EN10, Km 139.7, 2695-066 Bobadela LRS, Portugal
[e] ESTSetúbal, CDP2T, Instituto Politécnico de Setúbal, Campus do IPS, 2910 Setúbal, Portugal
[f] IDMEC, Instituto Superior Técnico, Universidade de Lisboa, Av. Rovisco Pais, 1049-001 Lisboa, Portugal
[g] CQE Instituto Superior Técnico, Universidade de Lisboa, Av. Rovisco Pais, 1049-001 Lisboa, Portugal

ARTICLE INFO

Keywords:
Polylactic acid 3D-platform
Iron oxide nanoparticles
Superparamagnetic
Nanohydroxyapatite
Antibacterial
Bone regeneration

ABSTRACT

Polymeric platforms obtained by three-dimensional (3D) printing are becoming increasingly important as multifunctional therapeutic systems for bone treatment applications. In particularly, researchers aim to control bacterial biofilm on these 3D-platforms and enhance re-growing bone tissue, at the same time. This study aimed to fabricate a 3D-printed polylactic acid platform loaded with hydroxyapatite (HA), iron oxide nanoparticles (IONPs) and an antibiotic (minocycline) with tuneable properties and multistimuli response. IONPs were produced by a facile chemical co-precipitation method showing an average diameter between 11 and 15 nm and a superparamagnetic behaviour which was preserved when loaded into the 3D-platforms. The presence of two types of nanoparticles (IONPs and HA) modify the nanomorphological/nanotopographical feature of the 3D-platforms justifying their adequate bioactivity profile and *in vitro* cellular effects on immortalized and primary osteoblasts, including cytocompatibility and increased osteogenesis-related gene expression (RUNX2, BGLAP and SPP1). Disk diffusion assays and SEM analysis confirmed the effect of the 3D-platforms loaded with minocycline against *Staphylococcus aureus*. Altogether results showed that fabricated 3D-platforms combined the exact therapeutic antibiofilm dose of the antibiotic against *S. aureus*, with the enhanced osteogenic stimulation of the HA and IONPs nanoparticles which is a disruptive approach for bone targeting applications.

1. Introduction

Guided controlled delivery of bioactive substances and drugs to the bone is an area of intense research aiming to engineer delivery platforms that at the same time can have a therapeutic role on bone diseases such as infection or cancer along with the activation of bone regeneration processes (Wan et al., 2015).

Among those platforms, the three dimensional (3D) structures known as 3D-platforms are being explored as they can offer a temporary framework providing a suitable environment for cell adhesion and growth and thereby aiding in bone regeneration and at the same time providing a valuable platform for local *in situ* effects or delivery strategies (Chocholata et al., 2019).

Among different bioactive substances with potential interest to be present on the 3D-platforms are the superparamagnetic iron oxide nanoparticles (IONPs). In particular, IONPs are being investigated for

* Corresponding authors at: ESTSetúbal, CDP2T, Instituto Politécnico de Setúbal, Campus do IPS, 2910 Setúbal, Portugal. CQE Instituto Superior Tecnico, Universidade de Lisboa, Av. Rovisco Pais, 1049-001 Lisboa, Portugal (C.F. Santos). Research Institute for Medicines (iMed.ULisboa), Faculty of Pharmacy, Universidade de Lisboa, Avenida Prof. Gama Pinto, 1649-003 Lisboa, Portugal (A.F. Bettencourt).
E-mail addresses: catarina.santos@estsetubal.ips.pt (C.F. Santos), asimao@ff.ulisboa.pt (A.F. Bettencourt).
[1] Both contributed equally to this work.

https://doi.org/10.1016/j.ijpharm.2020.120097
Received 25 September 2020; Received in revised form 11 November 2020; Accepted 12 November 2020
Available online 17 November 2020

magnetic hyperthermia (Sneha and Sundaram, 2015; Zhang et al., 2014) and *peri*-implant osteomyelitis (Fang et al., 2017) treatments based on the generation of local heat under an alternating magnetic field (Dulińska-Litewka et al., 2019; Sneha and Sundaram, 2015; Zhang et al., 2014). Also, IONPs may present a significant interest in bone tissue regeneration as they exhibit osteoinductive properties promoting cell growth, proliferation, and the expression of osteogenic related genes (Ortolani et al., 2016; Zhang et al., 2014).

Despite IONPs interest, targeting these nanoparticles to the bone remains a challenge and the possibility of using 3D-platforms obtained by additive manufacturing techniques can offer new opportunities for their use. For example, De Santis et al., (2011) prepared by rapid prototyping poly-ε-caprolactone magnetic 3D-platforms embedding magnetite (Fe_3O_4) nanoparticles which promoted marked spreading of human mesenchymal stem cells. Using extrusion 3D-printing technology, a magnetic Fe_3O_4 mesoporous bioactive glass/polycaprolactone 3D-platform was developed by Zhang et al., (2014) showing potential multifunctionality related to the enhanced osteogenic activity and local anticancer drug (doxorubicin) delivery.

None of these studies, however, investigate the risk of the IONPs loaded 3D-platforms for promoting bone infection. Considering that bacteria often adhere to non-viable implanted materials in the form of dense structures known as biofilms, highly resistant to antibiotic treatment and being one of the pivotal causes for implant-associated infections (Martin et al., 2019), it is of paramount importance to evaluate the risk of IONPs loaded 3D-platforms to boost infections. Moreover, contradictory knowledge exists concerning the possible role of IONPs as an antimicrobial agent and specifically against biofilms (Dinali et al., 2017). For example, Sathyanarayanan et al., (2013) showed that IONPs reduce biofilm growth of *Staphylococcus aureus*, a main pathogen associated to bone infections. However, a study by Abdul et al., (2019) has shown that IONPs have no antibiofilm activity against *S. aureus* within 20 h, except at very high concentration (50 mg/mL), which is not adequate to human application due to toxicity effects. Therefore, this could be a matter of concern for the medical application of IONPs loaded 3D-platforms.

Here, it was fabricated a uniformed sized 3D-platform loaded with drug and multi bioactive nanoparticles to promote the repair and regrowing of bone tissue. For that, 3D-platforms were produced by an additive manufacturing method and the used IONPs and HA nanoparticles, were synthetized by a simple and cost-effective methodology, merging their potential multiple positive effects in the context of bone disorders.

As a first step of the present work, the main properties of the IONPs were assessed. Then, the characteristics of the designed composite 3D-platforms including physico-chemical, bioactivity, antibacterial response against *S. aureus*, cytocompatibility and osteogenic effects on MG-63 and human bone marrow stromal cells were evaluated. According to fine adjustment of 3D surface composition and arrangement, it was possible to develop a 3D bioactive composite carrier platform that allowed the bone cell multiplication and differentiation and maintained IONPs magnetic functional usage with antibacterial effects.

2. Materials and methods

2.1. IONPs preparation and characterization

IONPs were prepared by a facile chemical co-precipitation method, in aqueous medium at room temperature. Briefly, an iron chloride tetrahydrate solution (0.02 M), was mixed with an iron (III) chloride anhydrous solution (0.01 M) with molar ratio of [Fe(II) / Fe(III)] = 2:1. To guarantee a low oxygen environment during the co-precipitation, nitrogen (N_2) gas bubbled through the solution during 5 min. Afterwards, ammonia (25% V/V) was added to keep the pH close to 9.6. The suspension of IONPs instantaneously formed was filtered through a 0.22 μm membrane and washed with purified water. Finally, the obtained IONPs were dried at room temperature in a desiccator. The morphology of IONPs was characterized by transmission electron microscopy (TEM). IONPs were dropped (~2 μL) onto carbon-coated copper grids and examined by TEM using a Hitachi H-8100 microscope with a LaB6 filament operated at 200 kV and with a Keenview CCD bottom-mounted camera from Olympus. The distribution size was measured from TEM images and was based on the analysis of more than 100 IONPs in various images. The crystal structure of the IONPs was analysed by X-ray diffraction (XRD; Bruker D8 ADVANCE Powder Diffractometer) with monochromatic CuKα (target) radiation (1.5405 Å) in the 2-theta range from 10° to 70° and at a scan rate of 0.02°/min.

Magnetic characterization of IONPs was performed by magnetometry using a 6.5 T S700X SQUID (Cryogenic Ltd.) magnetometer. For all samples, the direct current (DC) magnetization was measured as a function of temperature (within the range 5–300 K), after both zero-field-cooling (ZFC) and field-cooling (FC) procedures. The static magnetic field used for the ZFC/FC measurements was 25 Oe. Isothermal magnetization curves were obtained for fields up to 5 T at temperatures ranging between 4 and 300 K. In the case of isolated IONPs, alternate current (AC) susceptibility measurements were also performed using the magnetic characterization system Maglab 2000 (Oxford Instruments). The in-phase (χ') and out-of-phase (χ'') linear susceptibilities were measured at frequencies 995, 4995, 6750, and 9995 Hz in the temperature range of 5–300 K, with an AC driving field of 5 Oe. Mössbauer spectra of the IONPs sample were collected at room temperature and 4 K in transmission mode using a conventional constant acceleration spectrometer and a 25-mCi ^{57}Co source in Rh matrix. The velocity scale was calibrated using an α-Fe foil at room temperature. Isomer shift values, IS, are given relative to this standard. The low-temperature measurement was performed with the sample immersed in liquid He in a bath cryostat. The spectra were fitted to Lorentzian lines using a non-linear least-squares method (Waerenborgh et al., 2005).

2.2. 3D-platforms printing, functionalization, and characterization

The delivery systems (3D-printed platforms) were produced by a previously optimized methodology by the team (Martin et al., 2019). Briefly, the 3D-platforms (width = 8 mm; length = 8 mm; height = 7.2 mm and square pores around 1000 ± 30 μm in axial direction) were printed through fused deposition modelling (FDM) using a BQ Prusa i3 Hephestos (BQ, Spain) by the extrusion of a polylactic acid (PLA) filament with 1.75 mm of diameter and a molecular weight of 60,000–80,000 g/mol (Real PLA, Netherlands). The 3D-printed platforms were subjected to alkaline hydrolysis by immersion in a 1:1 NaOH (0.25 M) and ethanol 96% (V/V) solution at room temperature with 200 rpm stirring (LD-40, Labinco) for 4 h. After this period, the 3D-platforms were washed with citric acid 0.5% (w/V) and deionized water. Subsequently, all the 3D-platforms were soaked for 24 h, at room temperature, with 200 rpm stirring (LD-40, Labinco) in an aqueous solution (1 mL) containing collagen (5 mg/mL, a gift from Dra Mădălina Kaya, Department of Collagen Research, Romania) and nanosized hydroxyapatite (HA, 5 mg/mL, synthesized by a hydrothermal method reported elsewhere) (Santos et al., 2012). Additionally, one set of 3D-platforms was also loaded with IONPs (1 mg/mL) (3D-HA-IONPs) and another with IONPs (1 mg/mL) and minocycline (MH, 0.5 mg/mL, Atral Cipan, Portugal) named as 3D-HA-IONPs-MH.

2.2.1. Physicochemical characterization of the 3D-platforms

2.2.1.1. Morphological and chemical. The morphology of the 3D-platforms surface was analysed through scanning electron microscopy (SEM) using a JEOL JSM-7001F equipment, with an energy beam of 20 kV, with a working distance of 10 mm and a collecting time of 50 s. The analysis of the surface elemental chemical composition was conducted by the respective energy dispersive X-ray (EDS). The dried 3D-platforms

were coated with a thin layer of conductive mixture of gold (Au) and palladium (Pd) to increase the conductivity of the samples. The presence of HA and IONPs was identified through Attenuated Total Reflection Fourier-transform Infrared Spectroscopy analysis, using an ATR-FTIR, Nicolet 5700, Thermo Electron Corporation. For ATR-FTIR measurements all 3D-platforms were placed on the ATR diamond crystal, and the spectra were obtained in the range of 4000–800 cm^{-1} resulting from an average of 128 scans collected with a resolution of 8 cm^{-1}.

2.2.1.2. Magnetic properties. Static magnetic properties by means of ZFC/FC measurements and isothermal magnetization curves were conducted on the 3D-platform in the same conditions described above for isolated IONPs (2.1.).

2.2.1.3. Bioactivity. The resulting 3D-platforms were immersed in Simulated Body Fluid (SBF) for up to 28 days to evaluate their bioactivity in a physiological like environment. SBF was prepared as reported by Kokubo and Takadama (2006). In brief, four specimens were immersed in 3 mL SBF and maintained in a 37 °C water bath with light shaking. At each time point (7, 14 and 28 days), 3D-platforms were collected and rinsed with deionised water and dried at room temperature, and the pH of SBF solution was measured.

The formation of a bone-like apatite layer in the 3D-platforms' surface was analysed through ATR-FTIR (Nicolet 5700, Thermo Electron Corporation) and SEM equipped with EDS (JSM7001F JEOL equipment) with an energy beam of 20 kV. For SEM analysis, the developed 3D-platforms were coated with a thin layer of conductive mixture of Au and Pd.

2.2.2. 3D-platform's antimicrobial properties

2.2.2.1. Antibiotic release testing. Antibiotic release studies were conducted by immersing each individual minocycline loaded 3D-platform (3D-HA-IONPs-MH) in 3 mL of HEPES buffer (10 mM at pH 7.4, VWR chemicals). Subsequently, they were gently stirred at 250 rpm in a plate-shaker (LD-40, Labinco) at 37 °C. *In vitro* minocycline release over time (28 h) was determined by UV–vis analysis (FLUOstar Omega microplate reader, BMG Labtech), at 350 nm.

The drug release mechanism was evaluated through experimental data fitting to the "coupled mechanism" represented by the equation: $M_t = a + b(1\text{-}e^{-kt}) + ct^{1/2}$ (Frutos et al., 2010), where M_t denotes the fraction of drug released up to time *t*; k is a constant of the mathematical model; a, represents the burst effect on drug release; the parameters b and c represent the contributions (%) of the dissolution and diffusion processes to the release, respectively.

In parallel, to help elucidating the mechanism of antibiotic delivery in the first 24 h, the adsorption of the release media by the 3D-platforms was also tested. In brief, dried 3D-platforms were immersed in HEPES buffer at 37 °C and 250 rpm agitation. At each time set, the 3D-platforms were removed from the buffer and the excess solution removed. Adsorption ratios were determined gravimetrically in dry basis using the equation: Adsorption (%) = $(W\text{-}W_0)/W_0 \times 100$, where W is the 3D-platform's weight at a certain time and W_o is the 3D-platform's dried weight (Guo et al., 2017).

2.2.2.2. Antibacterial performance. The effectiveness of the 3D-platforms against *Staphylococcus aureus* ATCC® 25923™ was determined by agar diffusion and biofilm tests as previously described (Martin et al., 2019; Pontes et al., 2016). Shortly, for the agar diffusion assay, isolated colonies were suspended in Mueller Hinton Broth (MHB, Biokar Diagnostics, France) and diluted until achieving $\cong 1 \times 10^8$ CFU/mL. The inoculum was swabbed uniformly on Muller Hinton Agar (MHA, Biokar Diagnostics, France) plates. The tested 3D-platforms and filter-paper disks (6 mm diameter) with 10 μL of minocycline at 3 mg/mL (positive control) or 10 μL of sterile water (negative control) were placed on the agar surface. Next, the plates were incubated at 37 °C for 24 h and the inhibition zone diameters, were measured with a digital Vernier calliper.

For the biofilm assay, the 3D-platforms were fixed at the bottom of the wells in a 24-well plate under aseptic conditions. Isolated colonies of *S. aureus* were suspended in Brain Heart Infusion medium (BHI, Biokar Diagnostics, France) with glucose at 1% (w/V) and adjusted to 3×10^8 CFU/mL. A final inoculum concentration of 3×10^6 CFU/mL was added to each microplate well. After 24 h of incubation at 37 °C, samples were washed twice with 10 mM phosphate-buffered saline (PBS, Sigma-Aldrich) and the biofilm fixed with graded series of ethanol (ranging from 75% to 100%). Biofilm formation was evaluated by SEM analysis (JSM7001F JEOL) with an energy beam of 10 kV, after coating the samples.

2.2.3. In vitro biological characterization

2.2.3.1. Cell culture and seeding on the 3D-platforms. The human osteosarcoma cell line MG-63 (ATCC®CRL-1427™) was obtained from the American Type Culture Collection. 3D-platforms were seeded at 5.2×10^4 cells/cm^2, in 24-well plates (incubated at 37 °C in a humidified atmosphere with 5% CO_2). The culture medium (Gibco® RPMI 1640 from ThermoFisher, supplemented with 10% foetal bovine serum, 100 μg/mL streptomycin, 100 U/mL penicillin and 2 mM L-glutamine) was changed twice a week, up to 28 days, until approximately 80% confluence.

The human bone marrow derived mesenchymal stromal cells (hBMSCs) were isolated from human bone marrow withdrawn from bilateral punctures of the posterior iliac crests of normal volunteers and were acquired from a certified vendor (Lonza, Catalog #: PT-2501). 3D-platforms were seeded at 1×10^5 cells/cm^2, in 24-well plates (incubated at 37 °C in a humidified atmosphere with 5% CO_2). The culture medium (Gibco® α-MEM; from ThermoFisher, containing 10% inactivated foetal bovine, 100 U/mL of penicillin, 100 μg/mL streptomycin and 0.25 μg/mL amphotericin B) was changed twice weekly until approximately 80% confluence.

2.2.3.2. MG-63 cells testing. ***Metabolic activity/viability***

The metabolic activity/viability of the cells was measured, using the non- destructive resazurin assay (Alamar Blue assay) based on the conversion (reduction) of resazurin into the fluorescent by-product resorufin by metabolically active and viable cells (Ferreira et al., 2017). After 14, 21 and 28 days of culture, cell viability was determined by adding 5 mM of resazurin solution (Sigma-Aldrich) into each well. After 2 h of incubation at 37 °C, the supernatant of each sample was collected and the resazurin reduction was determined by measuring the fluorescence at 540 nm excitation and 590 nm emission wavelengths using a fluorescent microplate reader (FLUOstar Omega, BMG Labtech). The experiment was performed in triplicate.

Assessment of magnetization

For the assessment of the magnetic properties, after 28 days of incubation, the cell-seeded 3D-platforms were washed 3 times with PBS (Sigma-Aldrich) and 20 mM glycine (BioRAD) solution and were fixed with 4% paraformaldehyde (Sigma-Aldrich) for 10–15 min at room temperature. Further, cells were washed again 3 times with the same solution. Afterwards, the magnetic contributions of IONPs in 3D-platforms (3D-HA-IONPs and 3D-HA-IONPs-MH) were obtained from experimental data of DC measurements after correction using a blank 3D-platform (3D-HA) for each group as previously described in Section 2.1.

2.2.3.3. hBMSCs testing. ***Metabolic activity/viability***

The metabolic activity/viability of the cells grown within the 3D-platforms was measured by the resazurin assay, as previously described in 2.2.3.1. Data was presented in arbitrary units of fluorescence and blank samples (without cells) were used to normalize the

assay. Experience was performed in quintuplicates.

Cell morphology and cell/3D-platform interaction

The morphology of growing cells and the detailed cell interaction with 3D-platforms was examined by SEM. At each time point, cell-seeded 3D-platforms were washed with warm PBS (Sigma-Aldrich) and cells were fixed for 15 min with 1.5% (V/V) glutaraldehyde in 0.14 M sodium cacodylate pH 7.3 (both from Sigma-Aldrich). Samples were dehydrated through immersion for 30 min in a series of successive ethanol:water solutions (50, 60, 70, 80, 90, 95 and 100% v/v of ethanol), followed by critical point drying (CPD 7501, Polaron Range). The samples were coated by sputtering with a thin film of Au/Pd, using a SPI Module Sputter Coater equipment and imaged in a High resolution (Schottky) Environmental Scanning Electron Microscope with X-Ray Microanalysis and Electron Backscattered Diffraction analysis (Quanta 400 FEG ESEM/EDAX Genesis X4M) microscope, using a voltage of 5.00 kV. Experience was performed in triplicates.

Gene expression analysis

Total RNA was extracted with Trizol reagent (Invitrogen, Carlsbad) from cultures grown for 15 days, accordingly to the manufacturer's protocol. RNA concentration and quality were determined with NanoDrop (NanoDrop Technologies) and the purified RNA was reverse-transcribed to cDNA using QuantiTect Reverse Transcription Kit (Qiagen, Germany). Quantitative PCR was following performed in an iCycler iQ Real-time PCR system (Bio-Rad), with the QuantiTect SYBR green PCR Kit (Qiagen, Germany). The relative level of each gene was normalized to the expression of the house keeping gene (ACTB, actin beta) and calculated via the $2^{-\Delta\Delta Ct}$ method. Validated primer sequences for the assayed genes (i.e., RUNX2, BGLAP coding for osteocalcin and SPP1 coding for osteopontin) were acquired from BioRad: ACTB – Unique Assay ID: qhsaLED0214042, RUNX2 – Unique Assay ID: qHsaCED0044067; BGLAP – Unique Assay ID: qHsaCED0044067; SPP1 – Unique Assay ID: qOcuCED0010864. Experience was performed in triplicates.

2.3. Statistical analysis

Statistical analysis was conducted with GraphPad Prism 6.01 software. Data normality was determined by the Shapiro-Wilk test. For normal data sets, one-way ANOVA was performed, followed by multiple comparisons using Tukey's test. For non-parametric data sets, Kruskal-Wallis test was performed, followed by multiple comparisons using Dunn's tests. *P* values less than 0.05 were considered significant.

3. Results and discussion

3.1. Characterization of the IONPs

In the present work, a co-precipitation method using a low oxygen environment to reduce the oxidation of IONPs was selected to obtain crystalline IONPs with nanometric size and superparamagnetic behaviour. The nanoparticles formed immediately after the ammonium hydroxide solution was added (Fig. 1A.), display a strong dark black colour, characteristic of IONPs (Mahdavi et al., 2013). Fig. 1A. and B. shows SEM and TEM images of the IONPs, respectively. It is clearly observed that IONPs presented a spherical shape with an average diameter of approximately 15 ± 3 nm as documented by the particle-size distribution curve obtained by TEM measurements (Fig. 1C.). Distinct rings in SAED pattern (inset in Fig. 1B.) characteristic of polycrystalline magnetite phase were also observed in IONPs (Martínez-Mera et al., 2007).

The crystalline phase of IONPs is revealed by the XRD pattern shown in Fig. 1D. The peaks of the XRD patterns of the IONPs can be attributed to magnetite Fe_3O_4 (JCPDS no. 19–0629) and/or maghemite γ-Fe_2O_3 (JCPDS no. 39–1346). It is difficult to distinguish by XRD the Fe_3O_4 from γ-Fe_2O_3 since both have similar crystal structure and the diffractogram of γ-Fe_2O_3 is virtually identical to that of Fe_3O_4 (Wu et al., 2015). In this case, diffraction peaks are broad due to the nanometric particle size and most likely a mixture of γ-Fe_2O_3 and Fe_3O_4 domains are present. ^{57}Fe Mössbauer spectroscopy measurements were carried out in order to better characterize the IONPs, based on the ion valence states.

The Mössbauer spectra of the IONPs (Fig. A.1, Appendix A) show six asymmetrically broadened absorption peaks. At 4 K these peaks are significantly narrower. These features are consistent with superparamagnetic behaviour of nanosized Fe oxides as explained in detail in (Mørup, 1987). The spectra may be properly analysed if three magnetic splittings are considered. At room temperature one of the sextets is typical of the fast electron hopping observed between Fe^{2+} and Fe^{3+} on the octahedral sites of magnetite above the Verwey transition (Table A1, Appendix A). These Fe cations are usually reported as $Fe^{2.5+}$ (Roca et al., 2007; Vandenberghe et al., 2000). At 4 K a sextet with significantly higher isomer shift, typical of Fe^{2+} (Roca et al., 2007), is observed. The estimated relative area of this sextet is approximately half the area of the $Fe^{2.5+}$ sextet detected at room temperature. This strongly suggests that, as expected, charge ordering has occurred in the magnetite domains below the Verwey transition observed in the magnetization data. The remaining two sextets observed at room temperature and 4 K are

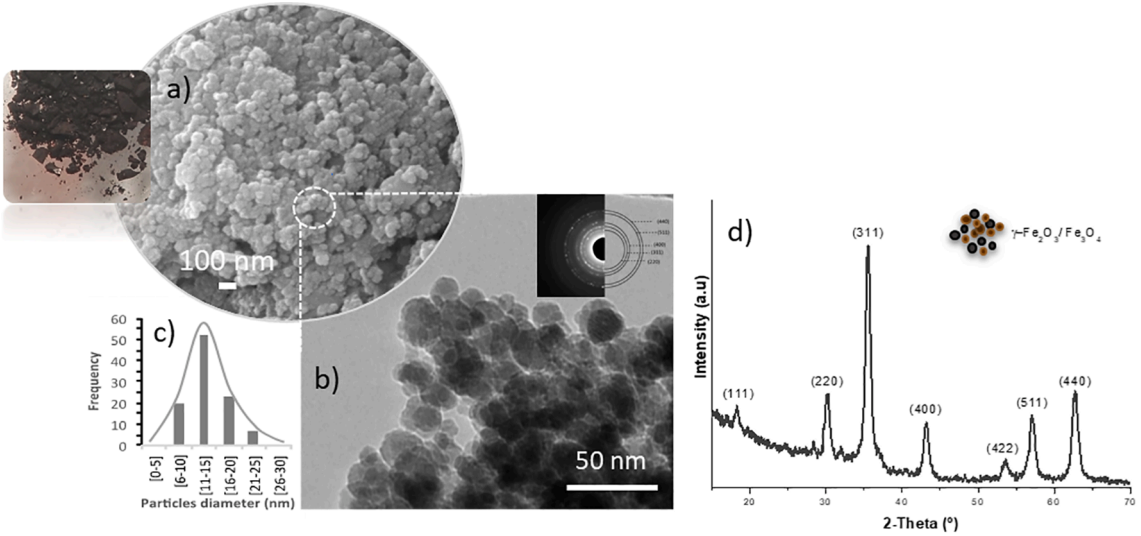

Fig. 1. A. Optical and SEM image of IONPs collected after precipitation; B. TEM image of IONPs showing the spherical like shape and the corresponding electron diffraction pattern (SAED) inset; C. IONPs size distribution; and D. X-ray diffraction pattern of IONPs.

consistent with Fe^{3+} on octahedral sites of maghemite and tetrahedral sites of both magnetite and maghemite domains. Mössbauer data show, therefore, that approximately 50% of the Fe cations are in magnetite domains while the remaining Fe cations are on maghemite domains.

Moreover, the formation of IONPs, may be explained by two separated reactions that could occur immediately as ammonium hydroxide solution is added to iron salts (Mahdavi et al., 2013) as described by the following chemical reactions.

$$Fe^{3+} + 3OH^- \rightarrow Fe(OH)_3$$

$$Fe(OH)_3 \rightarrow FeOOH + H_2O$$

$$Fe^{2+} + 2OH^- \rightarrow Fe(OH)_2$$

$$2FeOOH + Fe(OH)_2 \rightarrow Fe_3O_4\downarrow + 2H_2O$$

Since it was not possible to guarantee that the entire reaction has occurred free of oxygen, and having in mind the previous results, it can be considered that some magnetite nanoparticles were partially or completely oxidised to maghemite (γ-Fe_2O_3) (Mahdavi et al., 2013), and a mixture of iron oxides composed by Fe_3O_4, partially oxidized Fe_3O_4 and γ-Fe_2O_3 nanoparticles was obtained. Today, it is not yet clear which state presents more cytocompatibility. It has been stated that changes of Fe_3O_4 to γ-Fe_2O_3 could increase the toxicity against the stem cells, where Fe^{2+} ions released in the endosomes or lysosomes could catalyse Fenton-type reactions, leading to the formation of toxic radicals (Barrow et al., 2018). While, in another study, it was reported that magnetite induces higher toxicity when compared to maghemite in MH-S cells (Park et al., 2014). Considering these contradictory results reported in the literature, it can be pointed out that more studies are necessary to understand in detail the toxicity of IONPs.

Considering the importance of having IONPs with superparamagnetic behaviour, to increase the osteogenesis and the bone regeneration (Lu et al., 2018), magnetic measurements were also performed (Fig. 2). The magnetization of the IONPs was measured, as shown in Fig. 2B. At zero field (ZFC curve) the magnetic moments of the IONPs are randomly distributed, showing a very low net magnetic moment. On the contrary, when the sample is cooled under a magnetic field (FC curve) of 25 G, they start to align along the field direction, exhibiting a larger net moment. ZFC increases in all the range of measured temperatures, from 4 K up to 300 K, indicating that the magnetic moments gradually align along the magnetic field direction. An additional shoulder at temperature lower than 50 K is observed. This temperature is lower than the Verwey transition temperature observed for bulk magnetite with the ideal stoichiometry, 122–125 K, due to partial oxidation and/or small size of the magnetite particles (Goya et al., 2003; Matos et al., 2019; Vandenberghe et al., 2000). The irreversibility of the ZFC and FC data in all the range of measured temperatures confirms that these nanoparticles are superparamagnetic at room temperature. In fact, as revealed by the isothermal magnetization curves up to 5 T, the absence of both coercivity and remanence at 300 K (Fig. 2A.), confirms this behaviour while at low temperature, 10 K, a small coercive field, Hc, is observed (Fig. A.2., Appendix A). These IONPs show a high saturation magnetization, $Ms = 67$ emu/g, comparable with the values reported in the literature for magnetite nanoparticles (Goya et al., 2003) with similar average size and spherical shape (Fig. 1). The presence of slow magnetic relaxation revealed by the superparamagnetic behaviour of IONPs due to the interactions between small magnetic nanoparticles was also characterized by AC susceptibility (Huser et al., 1986; Mydosh, 1993). These temperature dependence measurements were performed at different frequency values under a zero magnetic static field. As shown in Fig. 2C. and D., both the in-phase, χ', and out-of-phase, χ'', components exhibit the expected superparamagnetic behaviour of IONPs systems, $\chi'(T)$ being easily comparable with the ZFC magnetization curve, while in $\chi''(T)$ a resolved peak around 35 K indicates the blocking temperature, which agrees well with the observed in the ZFC curve.

IONPs usually present a large surface-to volume ratio, which generally results in high chemical activity and loss of dispersibility (Kharisov et al., 2014). To avoid these effects, they are frequently coated or functionalized with organic or inorganic molecules (Guo et al., 2017; Kharisov et al., 2014; Li et al., 2017). An advantage of the present study was the incorporation of the IONPs in a collagen coating, which avoids this additional step, keeping their original physicochemical characteristics.

3.2. Characterization of the 3D-platforms

A 3D-printing technique combined with a simple coating method was applied to produce the 3D porous PLA structures (Martin et al., 2019). The 3D structures were coated with collagen, HA and IONPs (3D-HA-IONPs) or collagen, HA, IONPs and minocycline (3D-HA-IONPs-MH). 3D-platforms coated only with collagen and HA (3D-HA) were used as the control group. Fig. 3 allows following the colour evolution of the 3D-platforms after coating with different nanoparticles and antibiotic. The original beige colour of 3D-platform with HA (Fig. 3A.) gives way to a dark beige (Fig. 3D.), hence anticipating the presence of IONPs on 3D- platforms. The presence of minocycline (MH) was predicted by the characteristic yellowish colour (Martin et al., 2019) observed in the

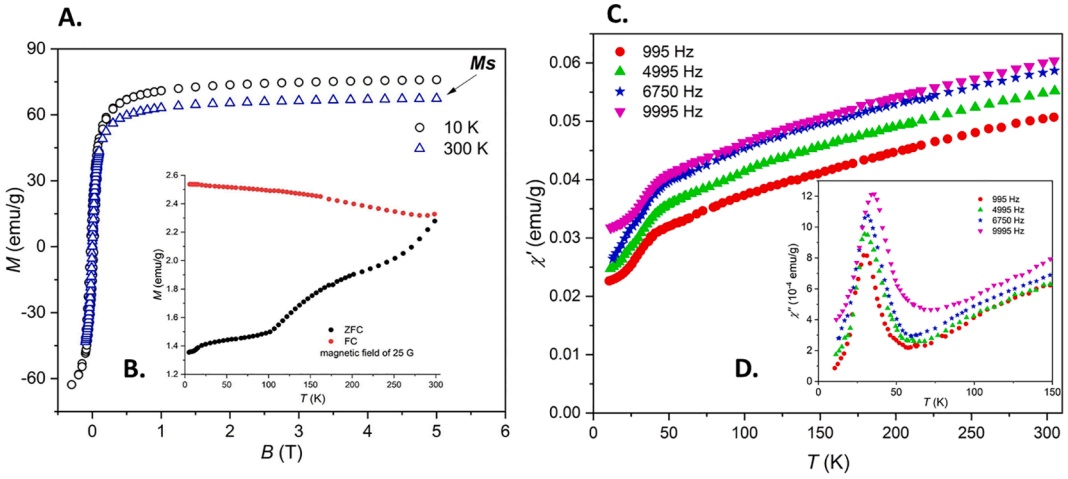

Fig. 2. IONPs magnetic properties. A. Magnetic field (B) dependence of magnetization (M) at 300 K and 10 K for IONPs showing the saturation of magnetization (Ms) at 5 Tesla; B. Temperature dependence of the zero-field cooling (ZFC) and field cooling (FC) magnetization at 25 G); C. and D. Temperature dependence of the AC susceptibility in-phase, χ', and out-of-phase components, χ'', at different frequencies.

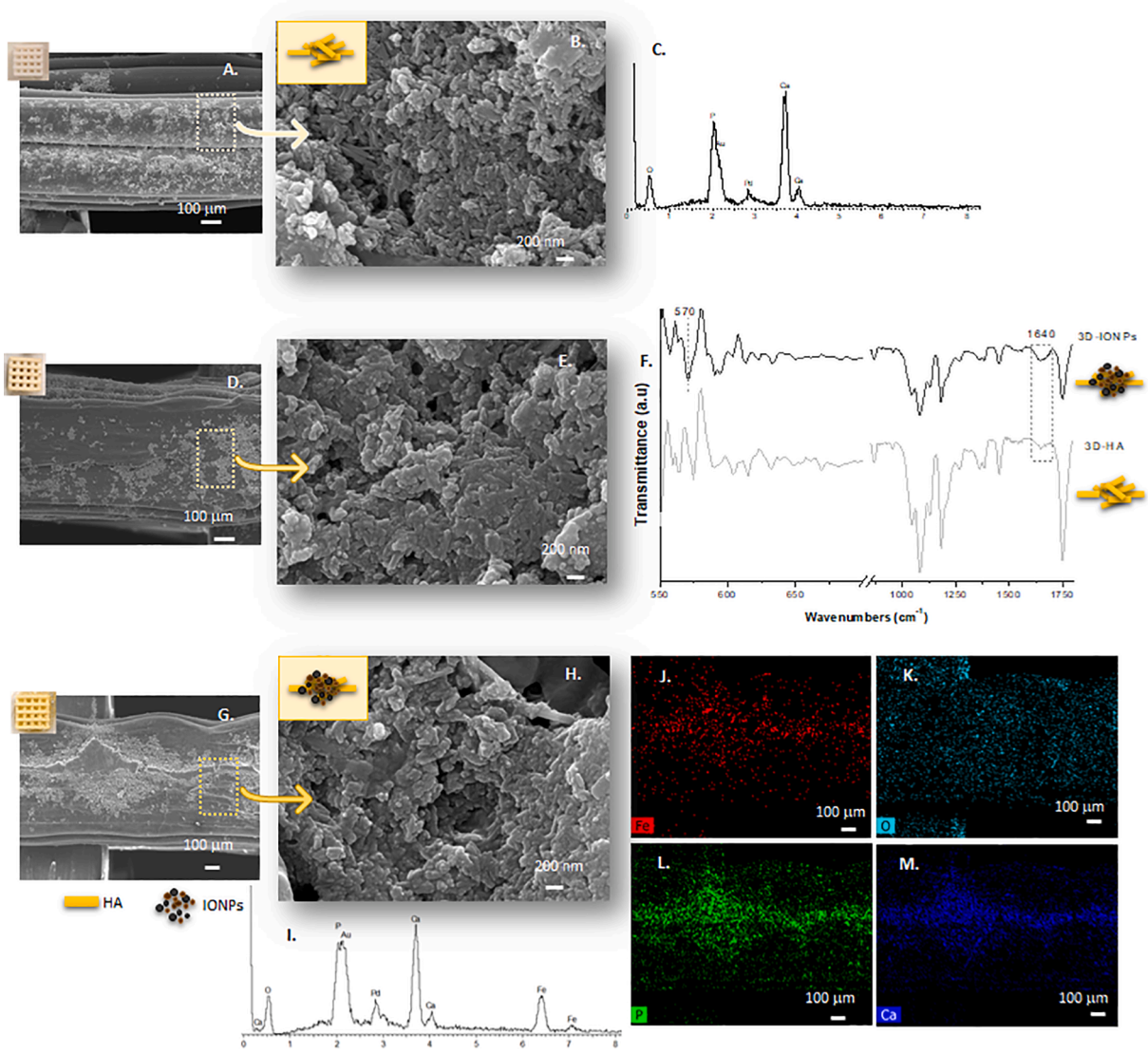

Fig. 3. SEM images of the 3D-HA (A. and B.) and respective EDS analysis showing the presence of Ca and P elements from HA (C.); SEM images of the 3D-HA-IONPs (D. and E.); ATR-FTIR spectra of the 3D-HA (light grey) and 3D-HA-IONPs (dark grey) with the evidence F-O band characteristic of IONPs (F.); SEM images of the 3D-HA-IONPs-MH platform (G. and H.); EDS analysis showing the presence of Fe, Ca, and P elements revelling the existence of IONPs and HA (I.); X-ray energy dispersive spectrometer (EDS) mapping of the 3D-HA-IONPs-MH platform showing the elementary distribution of Fe (J.), O (K.), P (L.) and Ca (M.).

3D-platform (Fig. 3G.). Further evidence of the presence of those nanoparticles on 3D-platforms is provided by the SEM images shown in Fig. 3A–C., wherein uniform rod like hydroxyapatite nanoparticles (Fig. 3B.) were identified and calcium and phosphorus elements, characteristics of HA were detected in EDS analysis (Fig. 3C.). Fig. 3D. and E. revealed the presence of nanoparticles with two distinct morphologies rod and spherical like, which correspond to HA and IONPs, respectively. The characteristic peaks of hydroxyapatite (HA), collagen and PLA were detected in the ATR-FTIR spectra of the 3D-HA and 3D-HA-IONPs as shown in Fig. 3F. (Martin et al., 2019; Santos et al., 2012). Further evidence of IONPs on 3D-platforms is provided by the ATR-FTIR spectrum, where the peak at 570 cm^{-1} was identified as Fe-O stretching vibration mode (Kostiv et al., 2017; Zhao et al., 2019).

The morphological characteristics of the 3D-HA-IONPs-MH platforms were analysed (Fig. 3G–H.), and the agglomeration of HA and IONPs nanoparticles is clearly observed on the surface. Although the minocycline becomes present, the composite coating preserves its integrity (Martin et al., 2019). The evidence of iron on 3D-HA-IONPs-MH platforms was confirmed by energy dispersive X-ray analysis (EDS), by the presence of two peaks at ~6.3 KeV and 7.2 KeV. The calcium and phosphorus elements from HA were also detected, as shown in Fig. 3I.

Considering the impact that chemical composition and/or elementary distribution can have on the biological response, EDS maps were performed on 3D-HA-IONPs-MH platforms. Fig. 3J–M. compares the EDS maps of 3D-HA-IONPs-MH with the corresponding SEM image (Fig. 3G.), with the details of elementary distribution of iron (Fe), calcium (Ca), phosphorus (P) and oxygen (O). A high concentration of iron (Fe) is detected in the same region of calcium (Ca) and phosphorus (P), although it has been also detected on the entire surface (Fig. 3J.).

A nanomorphological/nanotopographical feature on the 3D-platforms surface was observed due to the presence of those nanoparticles. Nanoscale topography could facilitate the cell adhesion, by providing anchoring sites and increase the cell migration and proliferation (Kim et al., 2012; Wang et al., 2016a).

The magnetic contributions of IONPs in the 3D-platforms were obtained from experimental data after corrections using a control, 3D-platform without IONPs (3D-HA), for each group, which evidenced a strong diamagnetic response. As shown in Fig. 4, the magnetic properties of IONPs in the 3D-platforms are quite similar to those of the original

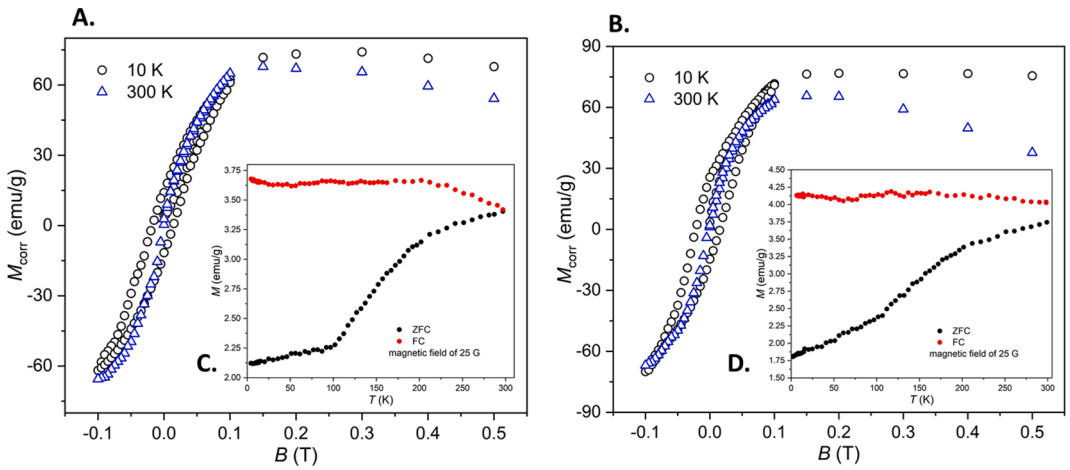

Fig. 4. 3D-HA-IONPs (A. and C.) and 3D-HA-IONPs-MH (B. and D.) platforms' magnetic properties. A. and B. Magnetic field (B) dependence of the corrected magnetization (Mcorr) at 300 K and 10 K for the 3D-HA-IONPs and 3D-HA-IONPs-MH platforms, respectively. C. and D. Temperature dependence of the zero-field cooling (ZFC) and field cooling (FC) magnetization at 25 G.

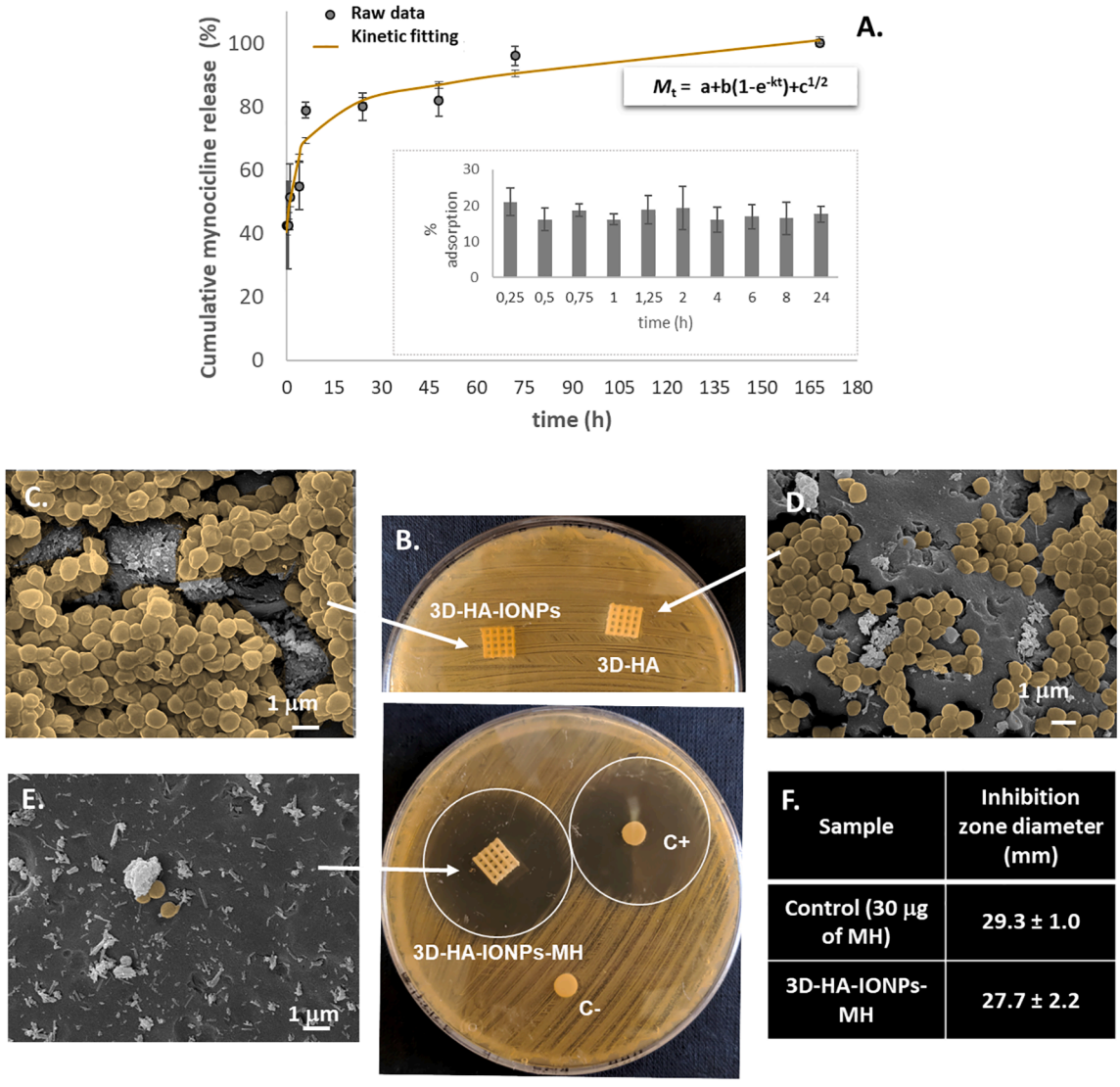

Fig. 5. *In vitro* antibiotic release assay (A.); line graph: release profile and kinetic fitting; bar graph: percentage of release media adsorption. Optical images of the agar diffusion assay (B.) of the 3D-platforms, of 30 µg of minocycline (positive control, C+) and distilled water (negative control, C−). SEM images, illustrating the *S. aureus* interaction with 3D-HA-IONPs (C.), 3D-HA (D.) and 3D-HA-IONPs-MH (E.); Inhibition zone diameter of the positive control and 3D-HA-IONPs-MH platform, resulting from the agar diffusion assay (F.).

isolated IONPs (Fig. 2A. and B.) which suggest that IONPs in these groups preserve the same magnetic behaviour. Assuming a similar saturation magnetization (*Ms* = 67 emu/g, and 65 emu/g, in 3D-HA-IONPs and 3D-HA-IONPs-MH, respectively) results suggest that the mass of IONPs adsorbed on 3D-HA-IONPs and 3D-HA-IONPs-MH platforms was approximately 2–3 μg.

3.3. Antibiotic delivery and antibacterial performance

The release profile of minocycline showed that most of the available drug was released by the 3D-HA-IONPs-MH platforms within 24 h (Fig. 5A.-line graph). Also, the antibiotic loaded 3D-platforms were able to restrict *S. aureus* growth as determined by the diameter of the inhibition zone measured in the agar diffusion test (Fig. 5B. and F.). Moreover, SEM analysis showed that biofilm was not present in the 3D-HA-IONPs-MH 3D-platform surface (Fig. 5E.). On the contrary, it should be noted that the other tested 3D-platforms (3D-HA and 3D-HA-IONPs) exhibited no antibacterial activity in the agar diffusion assay (Fig. 5B.), still favouring biofilm adhesion to the 3D-platforms surface (Fig. 5C. and D.).

The presence of nanoparticles (HA and IONPs) on the 3D-platforms surface (Fig. 3) can be responsible for boosting biofilm formation as bacteria adhesion can be promoted by the existence of these nanostructures due to their impact on nanoscale morphological and topographical features (Singh et al., 2011). Additionally, a possible antibacterial effect due to IONPs was not observed (Fig. 5B. and C.). The antimicrobial propensity of the IONPs is still not fully understood and studies point to controversial results, either positive or negative (Li et al., 2019). In the present study, the absence of activity against *S. aureus* observed by the 3D-HA-IONPs platforms can result from nanoparticles embedment in the collagen coating being, in this way (in the first hours), unavailable to be released and exert their potential antibacterial effects (Li et al., 2019).

In the case of the 3D-platforms loaded with the antibiotic, the nanotopographic effects may have been avoided by the rapid initial release of the minocycline from the collagen coating (Fig. 5A.line graph). According to the fitted kinetic model, a significant burst effect (parameter a = 26.8) was observed and confirmed in the drugs release profile, where a minocycline burst over 40% was observed in the first 15 min (Fig. 5A.line graph), corresponding to a concentration (2.9 ± 1.2 μg/mL), well above the minimum inhibitory concentration value for the tested *S. aureus* strain (0.5 μg/mL) (Matos et al., 2014). Moreover, the kinetic fitting showed that the antibiotic dissolution process (parameter b = 45.6) resulting from the rapid initial adsorption of water prevailed over the diffusion process (parameter c = 5) often related to changes in the inner 3D-platforms matrix porosity. This result might be attributed to the rapid adsorption by the collagen coating of the aqueous release media once the 3D-platforms were immersed (Fig. 5A.bar graph), reaching a stable percentage of about 20% within the remaining evaluated time. Also, the low molecular weight of minocycline (493.94), facilitates its rapid dissolution in the media (Matos et al., 2014). This high antibiotic release rate from collagen coating has long been documented and can be desirable to effectively prevent bacterial adhesion at initial hours after implantation, with no additional drug delivery that can contribute to induce and/or select resistant bacterial strains (van Vugt et al., 2018).

3.4. Bioactivity

The impact of the nanomorphology/nanotopography and chemical composition on the 3D-platforms bioactivity and stability was evaluated, in order to predict the so-called *in vivo* bone bioactivity. For that, the 3D-platforms were immersed in a SBF solution for up to 4 weeks and the obtained results are reported in Fig. 6. It is clearly visible in all ATR-FTIR spectra with nanoparticles (Fig. 6) the presence of two characteristic PO_4^{3-} absorption bands, one at 961 cm^{-1} and another at 1021 cm^{-1} which are ascribed to vibrations of P–O bonds (Santos et al., 2015, 2012). However, in the 3D-HA-IONPs spectrum the intensity of those PO_4^{3-} bands is more marked than in 3D-HA spectrum in the first 2 weeks of immersion (Fig. 6A.1–4). This may be explained by the presence of specific functional groups like hydroxyl, and phosphate which can favour the heterogenous nucleation and growth of bone-like apatite in SBF (Kato et al., 2015; Kim et al., 2005). Additionally, it is known that only the Fe_3O_4 and α-Fe_2O_3 induce calcium phosphate formation in SBF, since they can hydrolyse and form Fe-OH groups (Kato et al., 2015). So, the presence of these additional hydroxyl groups on the coating surface due to presence of Fe_3O_4 can, in a first stage, interact specifically with the positive ions like Ca^{2+} present in the SBF and form a Ca-rich layer which interact with the negative phosphate ions available. This mineralization process seems to be the responsible for the observed increase in the intensity of the phosphate vibration bands. Heterogenous nucleation and crystal growth on a coating requires chemical and physical affinities - the presence of IONPs seems to affect both. Indeed, the IONPs present in the coating change the nanotopography as observed in SEM results (Fig. 3H.) and surface composition (Fig. 3I.), inducing a great heterogeneous nucleation and a strong mineralization (Santos et al., 2015, 2012).

The mineralization process detected in ATR-FTIR results was accompanied by a significant increase in pH value, particularly in the first week (Fig. 6A.5). This pH variation detected was a consequence of the Ca-P layer formed on top of the 3D structures, similar results have been previously reported by Zhao et al., (2019).

The SEM images and EDS maps, as depicted in Fig. 6B., showed the mineralization of the 3D-HA-IONPs-MH platform along the 4 weeks. After one week, it can be observed the beginning of the mineralization process, with the formation of a non-uniform layer rich in calcium and phosphorus elements (Fig. 6B.1.1–1.6). When the immersion time was extended to 2 weeks, a uniform and dense Ca-P layer covering completely the 3D-platform was detected (Fig. 6B.2.1–2.6). After 3 weeks in SBF (Fig. 6B.3.1–3.6) it is still visible a superficial thin Ca-P layer on top of the 3D-platform. Nevertheless, the formation of the Ca-P layer implies both the uptake of different ions from SBF onto the 3D structure surface and the release of ions from the immersed 3D structures. The EDS maps revealed that during 3 weeks some IONPs agglomerates and are still detected in the 3D structures, meaning that the release of iron and degradation of the coating is a slow process. Finally, in the 4th week, the apatite layer present on top of the 3D-platform is almost invisible and the iron element was not detected (Fig. 6B.4.1–4.5). It indicated that the coating stability was compromised, and the degradation has begun. A schematic representation of the mineralization of 3D-HA-IONPs-MH platform along the time is presented in Fig. 6. A6.

3.5. In vitro biological characterization

It is known that 3D-platforms may come into direct contact with fibroblast, osteoblast, undifferentiated mesenchymal cells among other cell types, upon bone tissue implantation. Considered this, immortalized (MG-63) and undifferentiated mesenchymal (hBMSCs) cell lines were used to evaluate the biological properties, such as cytocompatibility and osteogenic effects of the developed 3D-platforms, as well as the maintenance of the magnetic properties after a long period of cell culture, mimicking the physiological milieu. Knowing that immortalized cell cultures have higher phenotypical stability compared to primary cells, they were selected to assess the magnetic properties of the 3D-platforms upon incubation with cells during 28 days (Vohra et al., 2008).

3.5.1. 3D-platforms biological response to immortalized osteoblastic cells

To guarantee that magnetic properties assessment was performed correctly, a pre-screening of the 3D-platforms' biological response was conducted. Results from cell viability using the Alamar Blue assay (Fig. 7A.) confirmed the cytocompatibility nature of the tested 3D-

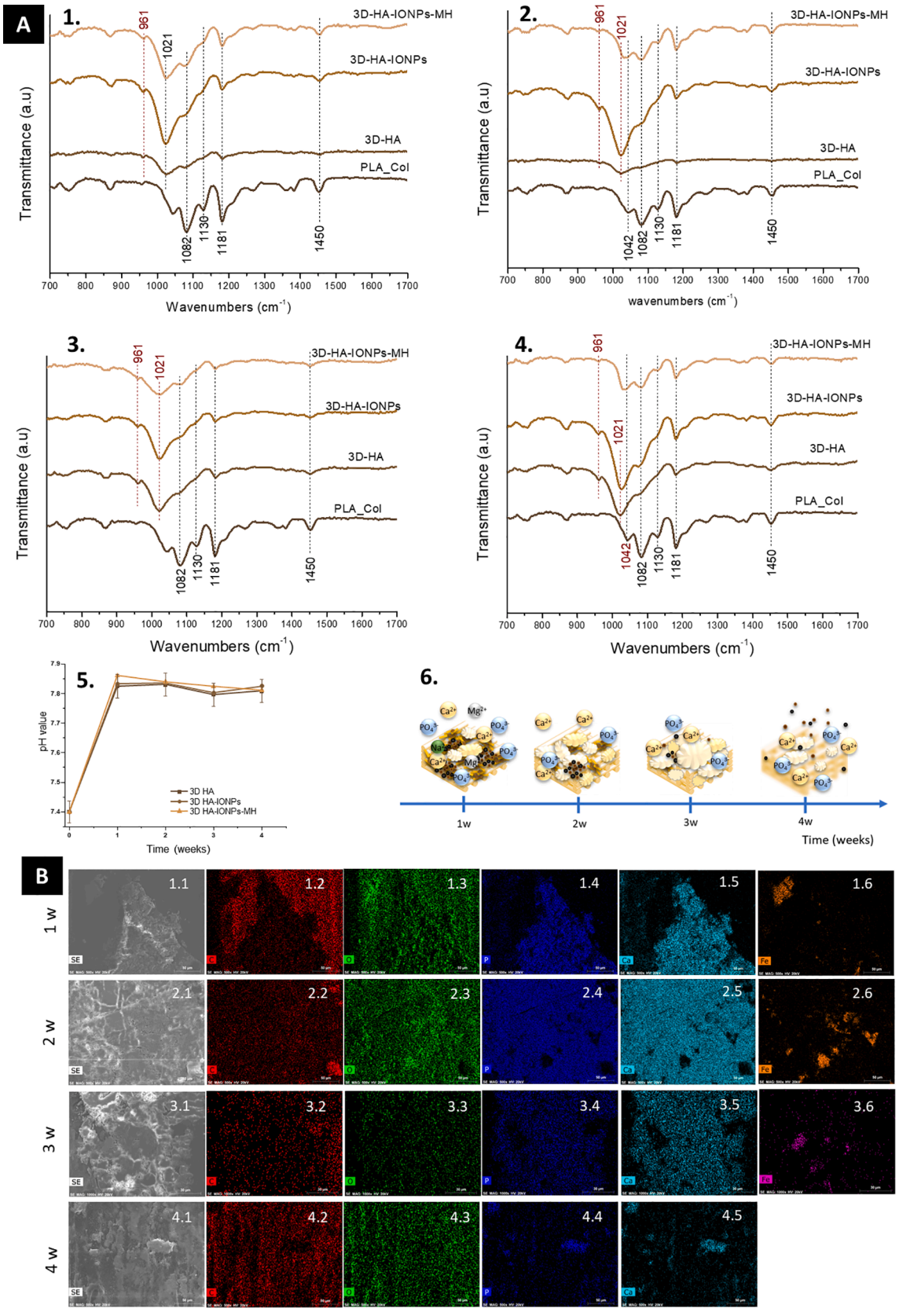

Fig. 6. A. ATR-FTIR spectra of 3D-platforms non-loaded and loaded with HA, HA and IONPs, and HA, IONPs and MH, after soaking in SBF for one (1.), two (2.), three (3.) and four (4.) weeks. pH value variation along the SBF soaking time (5.); Schematic representation of the mineralization of the 3D-HA-IONPs-MH platform along the 4 weeks in SBF (6.). B. X-ray.

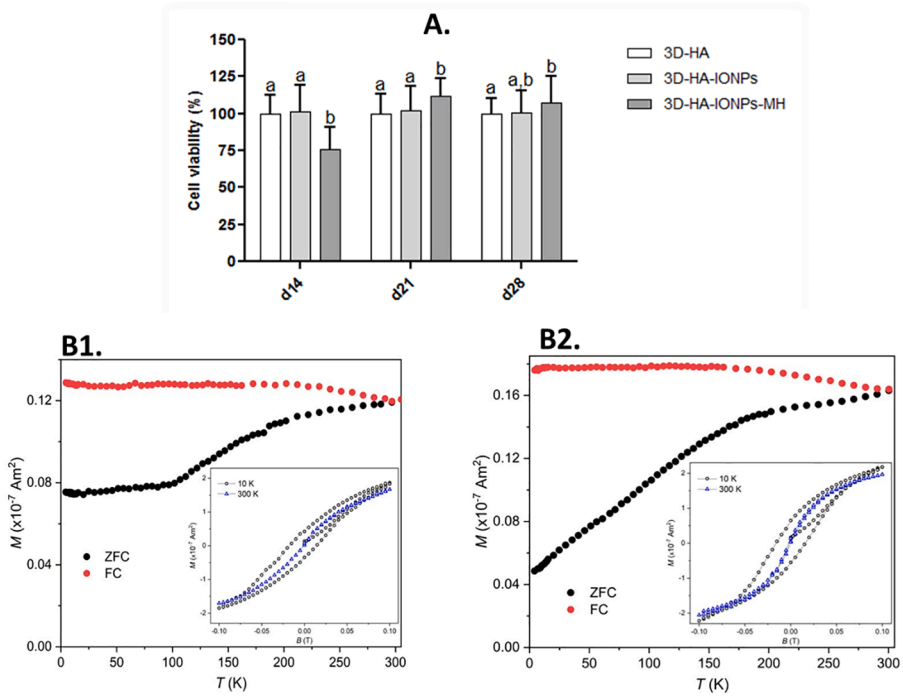

Fig. 7. Cytocompatibility (A.) and magnetic assessment (B.) of 3D-platforms up to 4 weeks culture with MG-63 cells. In A. different lowercase letters (a and b) indicate significant differences between the groups, with $p \leq 0.05$. B1. and B2. Temperature dependence of the zero-field cooling (ZFC) and field cooling (FC) magnetization for 3D-HA-IONPs and 3D-HA-IONPs-MH samples, respectively. Due to the impossibility of estimating the IONPs content present in both samples, magnetization, *M*, is shown in units of magnetic moment (Am^2) instead of mass magnetization (emu/g).

platforms for 28 days. Comparing to the control group (3D-HA), only the 3D-platforms containing minocycline had a slight effect on decreasing cells' viability in the first 2 weeks (Fig. 7A.), that can be due to the released antibiotic in high concentrations in the first hours as suggested by the minocycline release assay (Fig. 5A.line graph). Nevertheless, the cellular viability rapidly recovered over the subsequent weeks and even

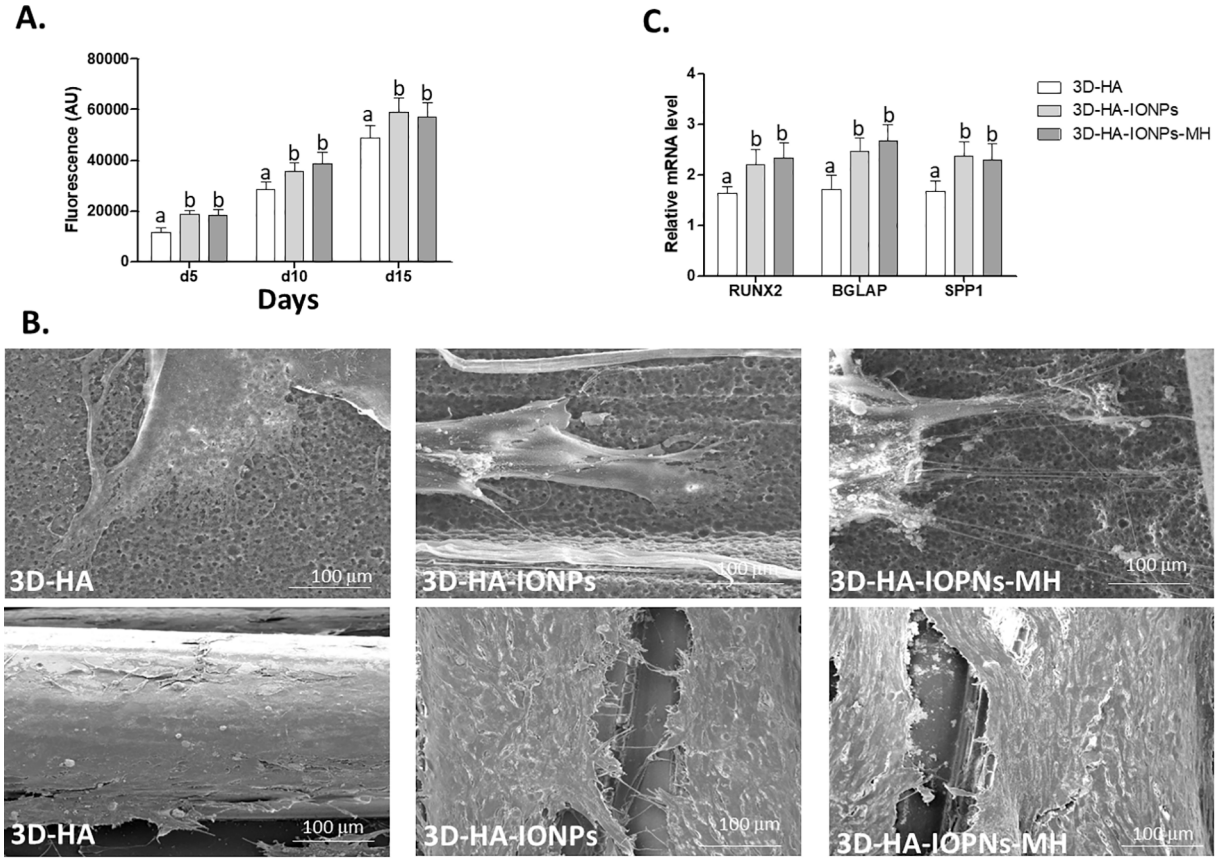

Fig. 8. Cytocompatibility assays with hBMSCs. A. Metabolic activity by resazurin assay, established for up to 15 days on the 3D-platforms. B. Representative SEM images of the cultures established for 5 (top row) and 15 (bottom row) days on the surface of PLA 3D-platforms. C. Relative expression of the osteogenesis-related genes RUNX2, BGLAP and SPP1. Note: different lowercase letters (a and b) indicate significant differences between the groups, with $p \leq 0.05$.

a slight increase was observed for the minocycline group for the 21 and 28 days' time points (Fig. 7A.), supporting an adequate biological response. These concentration-dependent minocycline cytocompatibility effects have also been suggested in other studies using human bone marrow osteoblastic cells (Gomes et al., 2008; Gomes and Fernandes, 2007).

In addition, it is interesting to note that the magnetic properties of 3D-platforms loaded with IONPs were still present following a long-term cell culture period, preserving their typical superparamagnetic behaviour (Fig. 7.B1 and B2). Although it is not possible to quantify the presence of IONPs, in both IONPs-loaded 3D-platforms, the magnetic behaviour is quite similar, with only slightly differences in the ZFC/FC plots, which may be due to different IONPs contents in each 3D-platform.

3.5.2. 3D-platforms biological response to primary hBMSCs cells

Biological processes, cellular interactions and molecular functions may be altered in immortalized cells, as comparing to non-modified populations, which may influence the outcomes of cytotoxicity and bioactivity evaluation. Additionally, information about the effects of 3D regenerative platforms on primary cells may be more reliable, compared to that attained with immortalized cell lines, allowing for more translational outputs. For all those reasons, in this work, in a second testing phase, primary human bone mesenchymal stromal cells (hBMSCs) were used to evaluate the biological properties of 3D-platforms in a more detailed approach, further embracing the osteogenic gene expression process (Vohra et al., 2008).

3.5.2.1. Cell viability/proliferation and cell/3D-platform interaction. hBMSCs cultures were established on the different 3D-platforms, and able to proliferate actively, up to the 15 days culture period, as sustained by the increasing resazurin values (Fig. 8A.) and SEM micrographs (Fig. 8B.). Cultures established on 3D-HA-IONPs and 3D-HA-IONPs-MH platforms presented increased values, as comparing to cultures established on control 3D-platforms (3D-HA), from day 5 onwards. No significant differences were attained between 3D-HA-IONPs and 3D-HA-IONPs-MH groups. SEM images of the cultures grown for 5 days revealed, for 3D-HA, broadly elongated flat cells with a high cytoplasmic spreading. 3D-platforms with IONPs revealed denser intercellular connections, with highly developed filopodial projections (with an increased number and extension) and enhanced cell-substrate interaction. At day 15, an organized cell monolayer of elongated and flat cells was established within the different groups, broadly covering the surface of the cell-seeded 3D-platforms.

3D-platforms loaded with IONPs – given the nanoparticles' distribution over the 3D-platforms' surface (Fig. 3) – are expected to display an increased surface area, further providing nanotopographic cues that allow for a selective deposition and conformational adaptation of recognizable molecules, able to tailor the cell adhesion process (Boyer et al., 2010; Jackson et al., 2018). Nanoscale morphology/topography seems to increase the mechanotransductive signalling into cells, enhancing the cellular anchoring to the substrate and consequently improving adhesion (Liu et al., 2016). In the present work, IONPs-loaded 3D-platforms elicited the formation and extension of filopodia (Fig. 8B.), supporting an increased cellular interaction with the substrate at the nanoscale, which facilitates the subsequent formation of cellular lamellipodia that is a crucial organizational step for cell spreading, migration and active proliferation (Dalby et al., 2014). IONPs addition further endowed 3D-platforms with superparamagnetic properties that, despite being regarded as nonmagnetic without the application of an external magnetic field, may still modulate the cellular functionality through residual magnetism-mediated effects (Sun et al., 2014). Attained data comes in line with that reported for the addition of IONPs to calcium phosphate 3D-platforms, revealing an increased osteoblastic adhesion and proliferation, as compared to control substrates (IONPs free), with differences attributed to the distinct surface geometrical and physic-chemical properties, and potential remanence, progressing from the IONPs' addition (Xia et al., 2019b). Further, minocycline addition to the 3D-platforms did not induce significant differences on the hBMSCs behaviour, regarding cells' adhesion and viability/proliferation.

3.5.2.2. Gene expression analysis - osteogenic differentiation. Established cultures were further characterized for gene expression analysis of relevant osteogenic markers, i.e. RUNX2, BGLAP and SPP1. RUNX2 is the furthest upstream transcription factor modulating the osteoblastic differentiation process, and a major regulator of osteogenesis, playing a determinant role in the osteogenic commitment of precursor populations and expression of lineage markers (Valenti et al., 2017). BGLAP codes for osteocalcin, a protein known to modulate the mineral species maturation for hydroxyapatite formation during the late osteogenic differentiation period, despite its relevant transcriptional signalling during the early stages of osteogenesis, confirming the osteogenic commitment (Valenti et al., 2017). SPP1 codes for osteopontin, one of the most predominant non-collagenous proteins of the extracellular matrix of the bone tissue, in which it plays a fundamental role in biomineralization (regulating apatite formation and growth), cell attachment and signalling (Valenti et al., 2017).

Comparatively to control (3D-HA), cultures established on 3D-HA-IONPs and 3D-HA-IONPs-MH platforms presented a significantly higher expression of the assayed osteogenic genes, with no significant differences between the latter groups (Fig. 8C.). The addition of IONPs to the 3D-platforms' composition seems to promote the osteogenic differentiation of precursor cells, given the increased expression of the major osteogenic transcription factor RUNX2, and two of its downstream factors (i.e. BGLAP, coding for osteocalcin; and SPP1, coding for osteopontin). IONPs, as distinctive nanointerfaces, may promote osteogenesis through distinct mechanisms, including mechanical stress signalling given the introduced nanomorphological/nanotopographical features, but further relying on the magneto-genetic response via activation of intracellular magnetoreceptors (Hao et al., 2019; Kotani et al., 2002). Magnetic field stimulation has been shown to prompt bone healing, stimulating cell proliferation and the induction of osteogenic differentiation in precursor populations, as demonstrated *in vitro* and *in vivo* (Kotani et al., 2002). In the present study, the addition of IONPs to the 3D-platforms' composition, given the conservation of a strong diamagnetic response even in the absence of an external magnetic field (Fig. 4. and 7. B1 and B2), could grant an endogenous magnetic field formation that prompts osteogenesis. Accordingly, IONPs addition to PLGA/PCL 3D-platforms greatly enhanced the osteogenic program of adipose-derived stem cells in the absence of an external magnetic field, far superiorly than the addition of similar gold nanoparticles, entailing the increased osteogenic outcome to the potential ferromagnetic activity of IONPs (Chen et al., 2018). Mechanistically, the IONPs-dependent osteogenic promotion is expected to be mediated by the WNT/β-catenin and MAPK pathways (Wang et al., 2016b; Xia et al., 2019a), fundamental signalling cascades involved in the osteogenic activation of hBMSCs and consequently, on the bone healing and regeneration processes (Hayrapetyan et al., 2015). Finally, the addition of minocycline to the 3D-platforms' composition was found not to interfere with the IONPs-mediated osteogenic induction.

4. Conclusions

This study reports for the first time the combination of superparamagnetic iron oxide and hydroxyapatite nanoparticles with minocycline in a 3D-printed platform for potential bone treatment applications where bacterial infection is of concern.

Besides assuring the maintenance of the magnetic properties of the IONPs, the proposed 3D-construct showed excellent bioactivity with the formation of an apatite layer on 3D-platforms surface, activity against

S. aureus as well as cytocompatibility and osteogenic effects on immortalized and primary bone cells.

The combination of new approach using nanoengineering to develop HA and IONPs and additive manufacturing method to produce the 3D-platform was crucial to design and tailor this 3D structure with multi-stimuli response and anti-bacterial activity with potential application in the context of bone diseases.

CRediT authorship contribution statement

Ana S. Saraiva: Investigation, Methodology, Writing - original draft. **Isabel A.C. Ribeiro:** Conceptualization, Methodology, Validation. **Maria H. Fernandes:** Formal analysis, Methodology, Validation. **Ana Cláudia Cerdeira:** Investigation, Formal analysis. **Bruno J.C. Vieira:** Investigation, Formal analysis. **João Carlos Waerenborgh:** Conceptualization, Investigation, Methodology, Validation. **Laura C.J. Pereira:** Conceptualization, Funding acquisition, Validation. **Ricardo Cláudio:** Investigation, Methodology, Validation. **Maria João Carmezim:** Conceptualization, Investigation, Methodology, Validation. **Pedro Gomes:** Conceptualization, Writing - review & editing, Supervision. **Lídia M. Gonçalves:** Conceptualization, Validation, Supervision. **Catarina F. Santos:** Conceptualization, Formal analysis, Methodology, Validation, Project Administration,Writing - review & editing, Supervision. **Ana F. Bettencourt:** Conceptualization, Funding acquisition, Project Administration, Validation, Writing - review & editing, Supervision.

Declaration of Competing Interest

The authors declare that they have no known competing financial interests or personal relationships that could have appeared to influence the work reported in this paper.

Acknowledgments

Support for this work was provided by National Funds through FCT - Fundação para a Ciência e Tecnologia, I.P, under the projects with references UIDB/04138/2020 and UIDP/04138/2020, PTDC/BTM-SAL/29335/2017, UIDB/50022/2020, CQE-UIDB/00100/2020, UIDB/50006/2020, UID/Multi/04349/2013, PDTC/QUI-QIN/32240/2017 and GCT grant to A.C.C. (BL156/2019_IST-ID).

Appendix A. Supplementary material

Supplementary data to this article can be found online at https://doi.org/10.1016/j.ijpharm.2020.120097.

References

Abdul, F., Subhi, H., Taher, N., Raheem, I., 2019. Activity of iron oxide nanoparticles-chitosan composite on bacterial biofilm formation. J. Pharm. Sci. Res. 11, 1126–1130. https://doi.org/10.14500/icpas2018.mim104.

Barrow, M., Taylor, A., Fuentes-Caparrós, A.M., Sharkey, J., Daniels, L.M., Mandal, P., Park, B.K., Murray, P., Rosseinsky, M.J., Adams, D.J., 2018. SPIONs for cell labelling and tracking using MRI: magnetite or maghemite? Biomater. Sci. 6 (1), 101–106. https://doi.org/10.1039/C7BM00515F.

Boyer, C., Whittaker, M.R., Bulmus, V., Liu, J., Davis, T.P., 2010. The design and utility of polymer-stabilized iron-oxide nanoparticles for nanomedicine applications. NPG Asia Mater. 2 (1), 23–30. https://doi.org/10.1038/asiamat.2010.6.

Chen, H., Sun, J., Wang, Z., Zhou, Y.i., Lou, Z., Chen, B.o., Wang, P., Guo, Z., Tang, H., Ma, J., Xia, Y., Gu, N., Zhang, F., 2018. Magnetic cell–scaffold interface constructed by superparamagnetic IONP enhanced osteogenesis of adipose-derived stem cells. ACS Appl. Mater. Interfaces 10 (51), 44279–44289. https://doi.org/10.1021/acsami.8b17427.s001.

Chocholata, P., Kulda, V., Babuska, V., 2019. Fabrication of scaffolds for bone-tissue regeneration. Materials (Basel) 12. https://doi.org/10.3390/ma12040568.

Dalby, M.J., Gadegaard, N., Oreffo, R.O.C., 2014. Harnessing nanotopography and integrin–matrix interactions to influence stem cell fate. Nature Mater. 13 (6), 558–569. https://doi.org/10.1038/nmat3980.

De Santis, R., Gloria, A., Russo, T., D'Amora, U., Zeppetelli, S., Dionigi, C., Sytcheva, A., Herrmannsdorfer, T., Dediu, V., Ambrosio, L., 2011. A basic approach toward the development of nanocomposite magnetic scaffolds for advanced bone tissue engineering. J. Appl. Polym. Sci. 122, 3599–3605.

Dinali, R., Ebrahiminezhad, A., Manley-Harris, M., Ghasemi, Y., Berenjian, A., 2017. Iron oxide nanoparticles in modern microbiology and biotechnology. Crit. Rev. Microbiol. 43 (4), 493–507. https://doi.org/10.1080/1040841X.2016.1267708.

Dulińska-Litewka, J., Łazarczyk, A., Hałubiec, P., Szafrański, O., Karnas, K., Karewicz, A., 2019. Superparamagnetic iron oxide nanoparticles-current and prospective medical applications. Materials (Basel) 12. https://doi.org/10.3390/ma12040617.

Fang, C.H., Tsai, P.I., Huang, S.W., Sun, J.S., Chang, J.Z.C., Shen, H.H., Chen, S.Y., Lin, F. H., Hsu, L.T., Chen, Y.C., 2017. Magnetic hyperthermia enhance the treatment efficacy of peri-implant osteomyelitis. BMC Infect. Dis. 17, 1–12. https://doi.org/10.1186/s12879-017-2621-4.

Ferreira, M., Rzhepishevska, O., Grenho, L., Malheiros, D., Gonçalves, L., Almeida, A.J., Jordão, L., Ribeiro, I.A., Ramstedt, M., Gomes, P., Bettencourt, A., 2017. Levofloxacin-loaded bone cement delivery system: highly effective against intracellular bacteria and Staphylococcus aureus biofilms. Int. J. Pharm. 532 (1), 241–248. https://doi.org/10.1016/j.ijpharm.2017.08.089.

Frutos, G., Pastor, J.Y., Martínez, N., Virto, M.R., Torrado, S., 2010. Influence of lactose addition to gentamicin-loaded acrylic bone cement on the kinetics of release of the antibiotic and the cement properties. Acta Biomater. 6 (3), 804–811. https://doi.org/10.1016/j.actbio.2009.08.028.

Gomes, P.S., Fernandes, M.H., 2007. Effect of therapeutic levels of doxycycline and minocycline in the proliferation and differentiation of human bone marrow osteoblastic cells. Arch. Oral Biol. 52 (3), 251–259. https://doi.org/10.1016/j.archoralbio.2006.10.005.

Gomes, P.S., Santos, J.D., Fernandes, M.H., 2008. Cell-induced response by tetracyclines on human bone marrow colonized hydroxyapatite and Bonelike®. Acta Biomater. 4 (3), 630–637. https://doi.org/10.1016/j.actbio.2007.12.006.

Goya, G.F., Berquó, T.S., Fonseca, F.C., Morales, M.P., 2003. Static and dynamic magnetic properties of spherical magnetite nanoparticles. J. Appl. Phys. 94 (5), 3520–3528. https://doi.org/10.1063/1.1599959.

Guo, Z., Yang, C., Zhou, Z., Chen, S., Li, F., 2017. Characterization of biodegradable poly (lactic acid) porous scaffolds prepared using selective enzymatic degradation for tissue engineering. RSC Adv. 7 (54), 34063–34070. https://doi.org/10.1039/C7RA03574H.

Hao, L., Li, L., Wang, P., Wang, Z., Shi, X., Guo, M., Zhang, P., 2019. Synergistic osteogenesis promoted by magnetically actuated nano-mechanical stimuli. Nanoscale 11 (48), 23423–23437. https://doi.org/10.1039/C9NR07170A.

Hayrapetyan, A., Jansen, J.A., van den Beucken, J.J.J.P., 2015. Signaling pathways involved in osteogenesis and their application for bone regenerative medicine. Tissue Eng. Part B: Rev. 21 (1), 75–87. https://doi.org/10.1089/ten.teb.2014.0119.

Huser, D., Duyneveldt, A.J.V., Nieuwenhuys, G.J., Mydosh, J.A., 1986. Phenomenological model for the frequency dependence of the susceptibility of spin glasses and related compounds. J. Phys. C: Solid State Phys. 19 (19), 3697–3717. https://doi.org/10.1088/0022-3719/19/19/023.

Jackson, R.J., Patrick, P.S., Page, K., Powell, M.J., Lythgoe, M.F., Miodownik, M.A., Parkin, I.P., Carmalt, C.J., Kalber, T.L., Bear, J.C., 2018. Chemically treated 3D printed polymer scaffolds for biomineral formation. ACS Omega 3 (4), 4342–4351. https://doi.org/10.1021/acsomega.8b00219.s001.

Kato, Y., Yokoi, T., Shin, E., Kim, I.Y., Kawashita, M., Kikuta, K., Ohtsuki, C., 2015. Calcium phosphate-forming ability of magnetite and related materials in a solution mimicking in vivo conditions. J. Asian Ceramic Soc. 3 (1), 44–49. https://doi.org/10.1016/j.jascer.2014.10.007.

Kharisov, B.I., Dias, H.V.R., Kharissova, O.V., Vázquez, A., Peña, Y., Gómez, I., 2014. Solubilization, dispersion and stabilization of magnetic nanoparticles in water and non-aqueous solvents: recent trends. RSC Adv. 4 (85), 45354–45381. https://doi.org/10.1039/C4RA06902A.

Kim, D.H., Provenzano, P.P., Smith, C.L., Levchenko, A., 2012. Matrix nanotopography as a regulator of cell function. J. Cell Biol. 197, 351–360. https://doi.org/10.1083/jcb.201108062.

Kim, H.-M., Himeno, T., Kokubo, T., Nakamura, T., 2005. Process and kinetics of bonelike apatite formation on sintered hydroxyapatite in a simulated body fluid. Biomaterials 26 (21), 4366–4373. https://doi.org/10.1016/j.biomaterials.2004.11.022.

Kokubo, T., Takadama, H., 2006. How useful is SBF in predicting in vivo bone bioactivity? Biomaterials 27 (15), 2907–2915. https://doi.org/10.1016/j.biomaterials.2006.01.017.

Kostiv, U., Patsula, V., Šlouf, M., Pongrac, I.M., Škokić, S., Radmilović, M.D., Pavičić, I., Vrček, I.V., Gajović, S., Horák, D., 2017. Physico-chemical characteristics, biocompatibility, and MRI applicability of novel monodisperse PEG-modified magnetic Fe3O4&SiO2 core-shell nanoparticles. RSC Adv. 7, 8786–8797. https://doi.org/10.1039/c7ra00224f.

Kotani, H., Kawaguchi, H., Shimoaka, T., Iwasaka, M., Ueno, S., Ozawa, H., Nakamura, K., Hoshi, K., 2002. Strong static magnetic field stimulates bone formation to a definite orientation in vitro and in vivo. J. Bone Mineral Res. 17 (10), 1814–1821. https://doi.org/10.1359/jbmr.2002.17.10.1814.

Li, J., Nickel, R., Wu, J., Lin, F., van Lierop, J., Liu, S., 2019. A new tool to attack biofilms: driving magnetic iron-oxide nanoparticles to disrupt the matrix. Nanoscale 11 (14), 6905–6915. https://doi.org/10.1039/C8NR09802F.

Li, K., Nejadnik, H., Daldrup-Link, H.E., 2017. Next-generation superparamagnetic iron oxide nanoparticles for cancer theranostics. Drug Discovery Today 22 (9), 1421–1429. https://doi.org/10.1016/j.drudis.2017.04.008.

Liu, Y., Liu, S., Luo, D., Xue, Z., Yang, X., Gu, L., Zhou, Y., Wang, T., 2016. Hierarchically staggered nanostructure of mineralized collagen as a bone-grafting scaffold. Adv. Mater. 28 (39), 8740–8748. https://doi.org/10.1002/adma.201602628.

Lu, J.-W., Yang, F., Ke, Q.-F., Xie, X.-T., Guo, Y.-P., 2018. Magnetic nanoparticles modified-porous scaffolds for bone regeneration and photothermal therapy against tumors. Nanomed.: Nanotechnol. Biol. Med. 14 (3), 811–822. https://doi.org/10.1016/j.nano.2017.12.025.

Mahdavi, M., Ahmad, M.B., Haron, M.J., Namvar, F., Nadi, B., Ab Rahman, M.Z., Amin, J., 2013. Synthesis, surface modification and characterisation of biocompatible magnetic iron oxide nanoparticles for biomedical applications. Molecules 18, 7533–7548. https://doi.org/10.3390/molecules18077533.

Martin, V., Ribeiro, I.A., Alves, M.M., Gonçalves, L., Claudio, R.A., Grenho, L., Fernandes, M.H., Gomes, P., Santos, C.F., Bettencourt, A.F., 2019. Engineering a multifunctional 3D-printed PLA-collagen-minocycline-nanoHydroxyapatite scaffold with combined antimicrobial and osteogenic effects for bone regeneration. Mater. Sci. Eng.: C 101, 15–26. https://doi.org/10.1016/j.msec.2019.03.056.

Martínez-Mera, I., Espinosa-Pesqueira, M.E., Pérez-Hernández, R., Arenas-Alatorre, J., 2007. Synthesis of magnetite (Fe3O4) nanoparticles without surfactants at room temperature. Mater. Lett. 61 (23-24), 4447–4451. https://doi.org/10.1016/j.matlet.2007.02.018.

Matos, A.C., Gonçalves, L.M., Rijo, P., Vaz, M.A., Almeida, A.J., Bettencourt, A.F., 2014. A novel modified acrylic bone cement matrix. A step forward on antibiotic delivery against multiresistant bacteria responsible for prosthetic joint infections. Mater. Sci. Eng.: C 38, 218–226. https://doi.org/10.1016/j.msec.2014.02.002.

Matos, J.C., Clara Gonçalves, M., Pereira, L.C.J., Vieira, B.J.C., Waerenborgh, J.C., 2019. SPIONS prepared in air through improved synthesis methodology: the influence of γ-Fe2O3/Fe3O4 ratio and coating composition on magnetic properties. Nanomaterials 9. https://doi.org/10.3390/nano9070943.

Mørup, S., 1987. Mössbauer effect studies of microcrystalline materials. In: Long, G.J. (Ed.), Mössbauer Spectroscopy Applied to Inorganic Chemistry. Plenum Press, New York, NY, USA.

Mydosh, J., 1993. Spin Glasses: An Experimental Introduction. Taylor & Francis.

Ortolani, A., Bianchi, M., Mosca, M., Caravelli, S., Fuiano, M., Marcacci, M., Russo, A., 2016. The prospective opportunities offered by magnetic scaffolds for bone tissue engineering: a review. Joints 04 (04), 228–235. https://doi.org/10.11138/jts/2016.4.4.228.

Park, E.-J., Umh, H.N., Choi, D.-H., Cho, M.H., Choi, W., Kim, S.-W., Kim, Y., Kim, J.-H., 2014. Magnetite- and maghemite-induced different toxicity in murine alveolar macrophage cells. Arch. Toxicol. 88 (8), 1607–1618. https://doi.org/10.1007/s00204-014-1210-1.

Pontes, C., Alves, M., Santos, C., Ribeiro, M.H., Gonçalves, L., Bettencourt, A.F., Ribeiro, I.A.C., 2016. Can Sophorolipids prevent biofilm formation on silicone catheter tubes? Int. J. Pharm. 513 (1-2), 697–708. https://doi.org/10.1016/j.ijpharm.2016.09.074.

Roca, A.G., Marco, J.F., Morales, M.D.P., Serna, C.J., 2007. Effect of nature and particle size on properties of uniform magnetite and maghemite nanoparticles. J. Phys. Chem. C 111 (50), 18577–18584. https://doi.org/10.1021/jp075133m.

Santos, C., Almeida, M.M., Costa, M.E., 2015. Morphological evolution of hydroxyapatite particles in the presence of different citrate: calcium ratios. Cryst. Growth Des. 15 (9), 4417–4426. https://doi.org/10.1021/acs.cgd.5b00737.

Santos, C., Gomes, P.S., Duarte, J.A., Franke, R.P., Almeida, M.M., Costa, M.E.V., Fernandes, M.H., 2012. Relevance of the sterilization-induced effects on the properties of different hydroxyapatite nanoparticles and assessment of the osteoblastic cell response. J. Roy. Soc. Interface 9 (77), 3397–3410. https://doi.org/10.1098/rsif.2012.0487.

Sathyanarayanan, M.B., Balachandranath, R., Genji Srinivasulu, Y., Kannaiyan, S.K., Subbiahdoss, G., 2013. The effect of gold and iron-oxide nanoparticles on biofilm-forming pathogens. ISRN Microbiol. 2013, 1–5. https://doi.org/10.1155/2013/272086.

Singh, A.V., Vyas, V., Patil, R., Sharma, V., Scopelliti, P.E., Bongiorno, G., Podestà, A., Lenardi, C., Gade, W.N., Milani, P., 2011. Quantitative characterization of the influence of the nanoscale morphology of nanostructured surfaces on bacterial adhesion and biofilm formation. PLoS ONE 6. https://doi.org/10.1371/journal.pone.0025029.

Sneha, M., Sundaram, N.M., 2015. Preparation and characterization of an iron oxide-hydroxyapatite nanocomposite for potential bone cancer therapy. Int. J. Nanomed. 10, 99–106. https://doi.org/10.2147/IJN.S79985.

Sun, J., Liu, X., Huang, J., Song, L., Chen, Z., Liu, H., Li, Y., Zhang, Y., Gu, N., 2014. Magnetic assembly-mediated enhancement of differentiation of mouse bone marrow cells cultured on magnetic colloidal assemblies. Sci. Rep. 4, 1–8. https://doi.org/10.1038/srep05125.

Valenti, M.T., Carbonare, L.D., Mottes, M., 2017. Osteogenic differentiation in healthy and pathological conditions. Int. J. Mol. Sci. 18 https://doi.org/10.3390/ijms18010041.

van Vugt, T.A.G., Walraven, J.M.B., Geurts, J.A.P., Arts, J.J.C., 2018. Antibiotic-loaded collagen sponges in clinical treatment of chronic osteomyelitis: a systematic review. J. Bone Joint Surg. 100 (24), 2153–2161. https://doi.org/10.2106/JBJS.17.01140.

Vandenberghe, R.E., Barrero, C.A., Da Costa, G.M., Van San, E., De Grave, E., 2000. Mössbauer characterization of iron oxides and (oxy)hydroxides: the present state of the art. Hyperfine Interact. 126, 247–259. https://doi.org/10.1023/A:1012603603203.

Vohra, S., Hennessy, K.M., Sawyer, A.A., Zhuo, Y.a., Bellis, S.L., 2008. Comparison of mesenchymal stem cell and osteosarcoma cell adhesion to hydroxyapatite. J. Mater. Sci. - Mater. Med. 19 (12), 3567–3574. https://doi.org/10.1007/s10856-008-3525-z.

Waerenborgh, J.C., Rojas, D.P., Shaula, A.L., Mather, G.C., Patrakeev, M.V., Kharton, V.V., Frade, J.R., 2005. Phase formation and iron oxidation states in SrFe(Al)O3−δ perovskites. Mater. Lett. 59 (13), 1644–1648. https://doi.org/10.1016/j.matlet.2005.01.033.

Wan, T., Stylios, G.K., Giannoudi, M., Giannoudis, P.V., 2015. Investigating a new drug delivery nano composite membrane system based on PVA/PCL and PVA/HA(PEG) for the controlled release of biopharmaceuticals for bone infections. Injury 46, S39–S43. https://doi.org/10.1016/S0020-1383(15)30053-X.

Wang, K., Bruce, A., Mezan, R., Kadiyala, A., Wang, L., Dawson, J., Rojanasakul, Y., Yang, Y., 2016a. Nanotopographical modulation of cell function through nuclear deformation. ACS Appl. Mater. Interfaces 8 (8), 5082–5092. https://doi.org/10.1021/acsami.5b10531.s001.

Wang, Q., Chen, B., Cao, M., Sun, J., Wu, H., Zhao, P., Xing, J., Yang, Y., Zhang, X., Ji, M., Gu, N., 2016b. Response of MAPK pathway to iron oxide nanoparticles in vitro treatment promotes osteogenic differentiation of hBMSCs. Biomaterials 86, 11–20. https://doi.org/10.1016/j.biomaterials.2016.02.004.

Wu, W., Wu, Z., Yu, T., Jiang, C., Kim, W.-S., 2015. Recent progress on magnetic iron oxide nanoparticles: synthesis, surface functional strategies and biomedical applications. Sci. Technol. Adv. Mater. 16 (2), 023501. https://doi.org/10.1088/1468-6996/16/2/023501.

Xia, Y., Guo, Y.u., Yang, Z., Chen, H., Ren, K.e., Weir, M.D., Chow, L.C., Reynolds, M.A., Zhang, F., Gu, N., Xu, H.H.K., 2019a. Iron oxide nanoparticle-calcium phosphate cement enhanced the osteogenic activities of stem cells through WNT/β-catenin signaling. Mater. Sci. Eng., C 104, 109955. https://doi.org/10.1016/j.msec.2019.109955.

Xia, Y., Zhao, Y., Zhang, F., Chen, B.o., Hu, X., Weir, M.D., Schneider, A., Jia, L.u., Gu, N., Xu, H.H.K., 2019b. Iron oxide nanoparticles in liquid or powder form enhanced osteogenesis via stem cells on injectable calcium phosphate scaffold. Nanomed. Nanotechnol. Biol. Med. 21, 102069. https://doi.org/10.1016/j.nano.2019.102069.

Zhang, J., Zhao, S., Zhu, M., Zhu, Y., Zhang, Y., Liu, Z., Zhang, C., 2014. 3D-printed magnetic Fe 3 O 4 /MBG/PCL composite scaffolds with multifunctionality of bone regeneration, local anticancer drug delivery and hyperthermia. J. Mater. Chem. B 2 (43), 7583–7595. https://doi.org/10.1039/C4TB01063A.

Zhao, Y., Fan, T., Chen, J., Su, J., Zhi, X., Pan, P., Zou, L., Zhang, Q., 2019. Magnetic bioinspired micro/nanostructured composite scaffold for bone regeneration. Colloids Surf., B 174, 70–79. https://doi.org/10.1016/j.colsurfb.2018.11.003.